

Accuracy of ghost-rotationally-invariant slave-boson theory for multi-orbital Hubbard model and realistic material

Tsung-Han Lee¹, Corey Melnick⁴, Ran Adler¹, Nicola Lanatà^{2,3}, Gabriel Kotliar^{1,4}

¹*Physics and Astronomy Department, Rutgers University, Piscataway, New Jersey 08854, USA*

²*School of Physics and Astronomy, Rochester Institute of Technology,
84 Lomb Memorial Drive, Rochester, New York 14623, USA*

³*Center for Computational Quantum Physics, Flatiron Institute, New York, New York 10010, USA and*

⁴*Condensed Matter Physics and Materials Science Department,
Brookhaven National Laboratory, Upton, New York 11973, USA*

We assess the accuracy of the ghost-rotationally-invariant slave-boson (g-RISB) theory in multi-orbital systems by applying it to both the three-orbital degenerate Hubbard model and a realistic Sr_2RuO_4 model extracted from first principle simulations, and comparing the results to those obtained using the dynamical mean-field theory (DMFT). Our findings indicate that g-RISB's accuracy can be systematically improved toward the exact DMFT limit in infinite dimensional multiorbital models by increasing the number of ghost orbitals. This allows for a more precise description of Hund's metal behavior and Mott transition compared to the original RISB approach. We also demonstrate that g-RISB reliably captures the quasiparticle weight, spectral functions, and Fermi surface for the realistic Sr_2RuO_4 model compared to DMFT. These results show the potential of g-RISB as a reliable tool for simulating correlated materials. The connection between the g-RISB and DMFT self-energy is also discussed.

I. INTRODUCTION

The rotationally-invariant slave-boson (RISB) mean-field theory¹, Gutzwiller approximation²⁻⁸, and other slave-particle mean-field approaches are efficient methodologies for studying the strong correlation effects in multiorbital Hubbard models⁹⁻¹⁴. These approaches effectively capture the fundamental orbital-selective Mott physics and Hund's metallicity in multiorbital systems, exhibiting qualitative agreement with the more computationally demanding dynamical mean-field theory (DMFT)¹⁵, and have been widely applied to investigate realistic materials, such as iron-based superconductors and heavy-fermion systems¹⁶⁻²². However, despite their success, the accuracy of slave-particle mean-field approaches and the Gutzwiller approximation is not always sufficient. For example, these approaches tend to overestimate critical Coulomb interaction for the Mott transition due to the lack of descriptions of the charge fluctuation in the Mott insulating phase²³. Hence, they require the use of larger Coulomb interactions to achieve experimentally observed Mott insulating behavior in transition metal compounds²¹. Additionally, recent studies on Sr_2RuO_4 indicate that RISB significantly underestimates the effective mass of electrons^{24,25}. Therefore, it is desirable to have a systematic route to improve the accuracy of RISB.

Recently, the ghost-rotationally-invariant slave-boson (g-RISB) approach has been developed to improve the accuracy of the original RISB method^{23,26,27}. The key concept of g-RISB is to enlarge the variational space of the original RISB by introducing auxiliary "ghost" degrees of freedom, where similar ideas have been developed simultaneously in different contexts of many-body approaches²⁸⁻³¹. It has been shown that g-RISB with two additional ghost orbitals provides a reliable description

of the Mott transition in single-orbital Hubbard and Anderson lattice models when compared to DMFT^{23,26,32}. Moreover, the studies on the one-band Hubbard model have shown that the accuracy of g-RISB can be systematically improved towards the exact solution in infinite dimensions by increasing the number of ghost orbitals³³⁻³⁵. However, the accuracy of g-RISB as the number of ghost orbitals increases has not been explored in multiorbital systems. Recently, the g-RISB has been applied to multiorbital systems focusing on the quasiparticle, spectral, and local atomic properties for multiorbital models on the Bethe lattice³⁶. However, the energetics and the application of g-RISB to more realistic models of materials have not been explored. In particular, it would be desirable to explore if g-RISB can solve the above-mentioned limitations of RISB, i.e., the overestimation of the critical Coulomb interaction of the Mott transition and the underestimation of the effective mass of Sr_2RuO_4 ^{21,24,25}.

In this work, we assess the accuracy of g-RISB on the degenerate three-orbital Hubbard model and the realistic Sr_2RuO_4 model extracted from first principle simulations, by comparing the results with DMFT. For the degenerate three-orbital model, we demonstrate that g-RISB significantly enhances the accuracy of the original RISB approach, providing a more precise description of Hund's metallic behavior and Mott transitions, where the critical point of the Mott transition is consistent with DMFT. Furthermore, we provide numerical evidence that the accuracy of g-RISB can be systematically improved toward the exact DMFT limit in infinite dimensions by increasing the number of ghost orbitals in the considered multiorbital models. For the realistic Sr_2RuO_4 model, our results illustrate that g-RISB captures the energy, spectral functions, Fermi surface, and quasiparticle weight in good agreement with DMFT and experiments. In addition, we discuss the connection be-

tween the g-RISB and DMFT self-energy. Our benchmarks highlight the potential of g-RISB as a reliable tool for simulating strongly correlated materials.

II. MODEL

We consider the following three-orbital Hubbard model

$$H = \sum_{\mathbf{k}} \sum_{ll'\sigma} \epsilon_{\mathbf{k}ll'} c_{\mathbf{k}l\sigma}^\dagger c_{\mathbf{k}l'\sigma} + \sum_{\mathbf{R}} H_{\mathbf{R}}^{\text{loc}} [\{c_{\mathbf{R}l\sigma}^\dagger, c_{\mathbf{R}l\sigma}\}], \quad (1)$$

where $c_{\mathbf{k}l\sigma}^\dagger$ and $c_{\mathbf{k}l\sigma}$ are the electronic creation and the annihilation operators, respectively, with the orbital index l , the spin index σ , the momentum index \mathbf{k} , and the site index \mathbf{R} , and $\epsilon_{\mathbf{k}ll'}$ is the hopping dispersion. In this work, we will focus on the $\epsilon_{\mathbf{k}ll'}$ corresponding to a degenerate semicircular density of state of the infinite dimension Bethe lattice and a realistic Sr_2RuO_4 dispersion extracted from the first principle simulations. The local Hamiltonian $H_{\mathbf{R}}^{\text{loc}}$ has the following form:

$$H_{\mathbf{R}}^{\text{loc}} [\{c_{\mathbf{R}l\sigma}^\dagger, c_{\mathbf{R}l\sigma}\}] = \sum_{ll'\sigma} \epsilon_{\mathbf{R},ll'}^\text{loc} c_{\mathbf{R}l\sigma}^\dagger c_{\mathbf{R}l'\sigma} + H_{\mathbf{R}}^{\text{int}} [\{c_{\mathbf{R}l\sigma}^\dagger, c_{\mathbf{R}l\sigma}\}], \quad (2)$$

where $\epsilon_{\mathbf{R},ll'}^\text{loc}$ is the local one-body interaction and

$$\begin{aligned} H_{\mathbf{R}}^{\text{int}} [\{c_{\mathbf{R}l\sigma}^\dagger, c_{\mathbf{R}l\sigma}\}] = & U \sum_l n_{\mathbf{R}l\uparrow} n_{\mathbf{R}l\downarrow} \\ & + U' \sum_{l < l', \sigma} n_{\mathbf{R}l\sigma} n_{\mathbf{R}l'\sigma} + (U' - J) \sum_{l < l', \sigma} n_{\mathbf{R}l\sigma} n_{\mathbf{R}l'\bar{\sigma}} \\ & - J \sum_{l < l'} (c_{\mathbf{R}l\uparrow}^\dagger c_{\mathbf{R}l'\downarrow} c_{\mathbf{R}l'\downarrow}^\dagger c_{\mathbf{R}l\uparrow} + c_{\mathbf{R}l\downarrow}^\dagger c_{\mathbf{R}l'\uparrow} c_{\mathbf{R}l'\uparrow}^\dagger c_{\mathbf{R}l\downarrow} \\ & + \text{H.c.}). \end{aligned} \quad (3)$$

is the Hubbard-Kanamori parameterization of the two-body Coulomb interaction³⁷. In addition, we use the rotationally-invariant condition $U' = U - 2J$. In the following, we will also introduce indices $\alpha \equiv (l, \sigma)$ to combine the electronic spin and orbital degrees of freedom.

III. METHODS

A. Ghost rotationally-invariant slave-boson

Here, we describe the formalism of g-RISB for multi-orbital models, which is the direct generalization of the previous works^{23,26,27,33}. The g-RISB theory is encoded in the following Lagrange function:

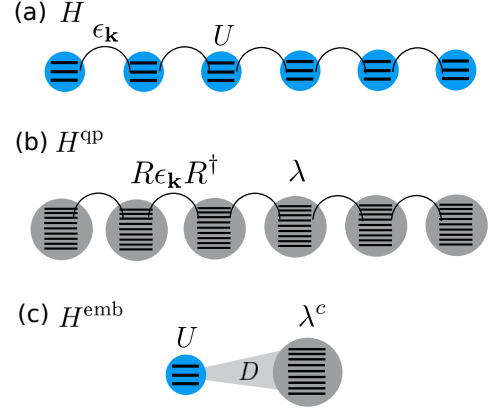


Figure 1. Schematic representation of the (a) original three-orbital Hubbard Hamiltonian H , (b) the non-interacting quasiparticle Hamiltonian H^{qp} including enlarged auxiliary ghost degrees of freedom with in total nine orbitals, and (c) the embedding Hamiltonian H^{emb} including an impurity with three orbitals and a bath with nine orbitals. The number of the orbitals in the bath of H^{emb} and in H^{qp} can be increased simultaneously by introducing more ghost orbitals to improve the g-RISB accuracy. Here we illustrate the Hamiltonians at bath size $N_b = 9$.

$$\begin{aligned} \mathcal{L}[\Phi, E^c; R, \lambda; D, \lambda^c; \Delta, \Psi_0, E] = & \frac{1}{N} \langle \Psi_0 | \hat{H}^{\text{qp}}[R, \lambda] | \Psi_0 \rangle \\ & + E(1 - \langle \Psi_0 | \Psi_0 \rangle) + \sum_i \left[\langle \Phi | \hat{H}^{\text{emb}}[D, \lambda^c] | \Phi \rangle \right. \\ & + E^c(1 - \langle \Phi | \Phi \rangle) \left. \right] - \sum_i \left[\sum_{ab} [\lambda + \lambda^c]_{ab} [\Delta]_{ab} \right. \\ & \left. + \sum_{c\alpha\alpha} ([D]_{a\alpha} [R]_{c\alpha} [\Delta(1 - \Delta)]_{ca}^{\frac{1}{2}} + \text{c.c.}) \right], \end{aligned} \quad (4)$$

where H^{qp} is the quasiparticle Hamiltonian, H^{emb} is the embedding Hamiltonian, and $|\Psi_0\rangle$ and $|\Phi_i\rangle$ are their corresponding wavefunction, respectively. The E and E^c are Lagrange multipliers enforcing the normalization of the wavefunctions. The λ and λ^c enforce the structure of the quasiparticle density matrix Δ , and D enforces the structure of the quasiparticle renormalization matrix R .

The quasiparticle Hamiltonian has the following form:

$$H^{\text{qp}} = \sum_{\mathbf{k}} \sum_{ab} \sum_{\alpha\beta} \left[R_{a\alpha} \epsilon_{\mathbf{k},\alpha\beta} R_{\beta b}^\dagger + \lambda_{ab} \right] f_{\mathbf{k}a}^\dagger f_{\mathbf{k}b}, \quad (5)$$

where, for the three-orbital model, $\alpha, \beta \in \{1 \uparrow, 1 \downarrow, 2 \uparrow, 2 \downarrow, 3 \uparrow, 3 \downarrow\}$ labels the original physical degrees of freedom $c_{\mathbf{k}\alpha}$, and a, b labels the auxiliary quasiparticle degrees of freedom $f_{\mathbf{k}a}$. The number of quasiparticle orbitals can be systematically increased by adding the so-called ghost orbitals to improve the accuracy of g-RISB. In this work, we used up to fifteen auxiliary quasiparticle orbitals, i.e., $a, b \in \{1 \uparrow, 1 \downarrow, \dots, 15 \uparrow, 15 \downarrow\}$ to study the

convergence of g-RISB in multiorbital Hubbard models. Note that with the minimal three quasiparticle orbitals, $a, b \in \{1 \uparrow, 1 \downarrow, 2 \uparrow, 2 \downarrow, 3 \uparrow, 3 \downarrow\}$, g-RISB recovers the original RISB approach.

The embedding Hamiltonian is as follows:

$$\hat{H}^{\text{emb}} = \hat{H}^{\text{loc}}[\{\hat{c}_\alpha^\dagger, \hat{c}_\alpha\}] + \sum_{a\alpha} \left(D_{a\alpha} \hat{c}_\alpha^\dagger \hat{f}_a + \text{h.c.} \right) + \sum_{ab} \lambda_{ab}^c \hat{f}_b \hat{f}_a^\dagger, \quad (6)$$

where \hat{c}_α^\dagger and \hat{c}_α are the impurity creation and annihilation operators, respectively, and \hat{f}_a^\dagger and \hat{f}_a are the bath creation and annihilation operators, respectively. We will use N_b to label the number of the bath orbitals. Note that the number of the bath orbital is the same as the number of the quasiparticle orbitals in H^{qp} . The schematic representation of the two models is shown in Fig. 1.

The stationary condition of the g-RISB Lagrange function leads to the following saddle-point equations:

$$\frac{1}{\mathcal{N}} \left[\sum_{\mathbf{k}} n_F(R\epsilon_{\mathbf{k}}R^\dagger + \lambda) \right]_{ba} = \Delta_{ab} \quad (7)$$

$$\frac{1}{\mathcal{N}} \left[\sum_{\mathbf{k}} \epsilon_{\mathbf{k}} R^\dagger n_F(R\epsilon_{\mathbf{k}}R^\dagger + \lambda) \right]_{ba} = \sum_{a\alpha} D_{c\alpha} [\Delta(I - \Delta)]_{ac}^{\frac{1}{2}} \quad (8)$$

$$\sum_{c\alpha} \frac{\partial}{\partial \Delta_{ab}} \left([\Delta(I - \Delta)]_{cd}^{\frac{1}{2}} D_{d\alpha} R_{c\alpha} + \text{c.c.} \right) + [\lambda + \lambda^c]_{ab} = 0 \quad (9)$$

$$\hat{H}^{\text{emb}}|\Phi\rangle = E^c|\Phi\rangle \quad (10)$$

$$\langle \Phi | \hat{c}_\alpha^\dagger \hat{f}_a | \Phi \rangle - \sum_c [\Delta(I - \Delta)]_{ac}^{\frac{1}{2}} R_{c\alpha} = 0 \quad (11)$$

$$\langle \Phi | \hat{f}_b \hat{f}_a^\dagger | \Phi \rangle - \Delta_{ab} = 0 \quad (12)$$

where n_F is the Fermi function, I is the identity matrix, and the variables R , λ , Δ , D , λ^c , and $|\Phi\rangle$ are determined self-consistently.

For the impurity solver of H_{emb} , we utilize the Lanczos exact-diagonalization (ED) algorithm to solve the ground state wavefunction $|\Phi\rangle$ for bath size $N_b \leq 9$. To explore the accuracy at larger bath size $N_b = 15$, it is necessary to utilize the density matrix renormalization group (DMRG) approach to solve the ground state wavefunction as the Hilbert space is too large for the Lanczos algorithm^{38–40}. In this work, we utilize the DMRG implemented in Block2 and PySCF as our impurity solver^{41–43}.

With the converged R and λ , one can compute the Green's function from

$$G_{\alpha\beta}(\mathbf{k}, \omega) = \sum_{ab} R_{a\alpha}^\dagger [(\omega + i0^+)I - R\epsilon_{\mathbf{k}}R^\dagger + \lambda]_{ab}^{-1} R_{b\beta} \quad (13)$$

and the self-energy can be determined from the Dyson equation

$$\Sigma_{\alpha\beta}(\omega) = [G_0^{-1}(\mathbf{k}, \omega) - G^{-1}(\mathbf{k}, \omega)]_{\alpha\beta}. \quad (14)$$

The quasiparticle renormalization weight is determined from

$$Z_{\alpha\beta} = \left[1 - \frac{\partial \text{Re}\Sigma(\omega)}{\partial \omega} \Big|_{\omega \rightarrow 0} \right]_{\alpha\beta}^{-1}. \quad (15)$$

An expression for the g-RISB self-energy has been derived in the previous work^{23,26}, resulting into a pole-expansion representation. In this work, we exploit the gauge freedom^{1,23,26} to provide a more compact expression, and provide further insight into the connection between RISB and the DMFT self-energy. Specifically, we choose a gauge transforming R and λ into the following block matrix form:

$$u^\dagger R = \tilde{R} = \begin{pmatrix} \tilde{R}_0 \\ 0 \end{pmatrix}, \quad u^\dagger \lambda u = \tilde{\lambda} = \begin{pmatrix} \tilde{\lambda}_0 & \tilde{\lambda}_1 \\ \tilde{\lambda}_1^\dagger & \tilde{\lambda}_2 \end{pmatrix}, \quad (16)$$

where u is the gauge transformation matrix^{1,20}, \tilde{R}^0 and $\tilde{\lambda}^0$ is square matrix of size $N \times N$, where N is the total number of physical spin orbitals. The matrix $\tilde{\lambda}_1$ is a $N \times M$ matrix where $M = N_b - N$, and $\tilde{\lambda}_2$ is a $M \times M$ diagonal matrix. From Eq. 13, one can show that the self-energy has the following form:

$$\Sigma_{\alpha\beta}(\omega) = \omega [I - [\tilde{R}_0^\dagger \tilde{R}_0]^{-1}]_{\alpha\beta} + \sum_{ab} [\tilde{R}_0]_{\alpha a}^{-1} [\tilde{\lambda}_0]_{ab} [\tilde{R}_0^\dagger]_{b\beta}^{-1} - [\epsilon^{\text{loc}}]_{\alpha\beta} + \sum_{abc} [\tilde{R}_0]_{\alpha a}^{-1} \frac{[\tilde{\lambda}_1]_{ac} [\tilde{\lambda}_1^\dagger]_{bc}}{[(\omega + i0^+)I - \tilde{\lambda}_2]_{cc}} [\tilde{R}_0^\dagger]_{b\beta}^{-1}. \quad (17)$$

In this work, we provide numerical evidence that $\tilde{R}^\dagger \tilde{R}$ approaches the identity as one increases the number of the ghost orbitals (see Appx. A). In this limit, the expression above simplifies further, as the first term in Eq. 17 vanishes. We have also checked numerically that $\Sigma(\infty)$ approaches the Hartree-Fock self-energy with increasing ghost orbitals (see Appx. A). The equation above, obtained from g-RISB principles, closely resembles the pole expansion proposed in previous DMFT literature⁴⁴.

B. Dynamical mean-field theory

We also perform the DMFT calculations to compare with g-RISB. To benchmark the accuracy with respect to the number of the bath orbitals, we utilize DMFT with the Lanczos ED solver (DMFT-ED) with discretized bath orbitals, which has been applied to multiorbital models^{45–51}. The hybridization function scheme is used for the bath fitting procedure with weight function $1/\omega_n$ ⁵², allowing stabler convergences for all the considered parameters. A fictitious temperature $\beta = 200$ is introduced for the bath fitting. The Lanczos algorithm is utilized to compute the ground state wavefunctions and Green's functions. In addition, we performed the DMFT calculations with the continuous-time quantum Monte Carlo (CTQMC) solver implemented in the TRIQS library, providing us the exact solution for the benchmark^{53,54}.

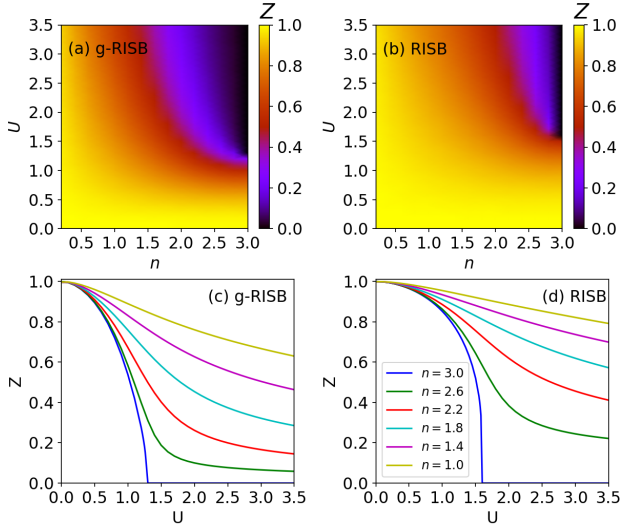


Figure 2. (a) and (c) the quasiparticle weight Z for the degenerate three-orbital Hubbard model on Bethe lattice from g-RISB with $N_b = 9$ bath orbitals. (b) and (d) the quasiparticle weight of RISB (g-RISB with $N_b = 3$) as a function of Coulomb interaction U with $J = 0.25U$ for different electron filling n .

IV. RESULTS

A. Degenerate three-orbital Hubbard model

We first apply the g-RISB approach to the degenerate three-orbital Hubbard model focusing on Hund's metal regime with Hund's coupling fixed at $J = 0.25U$, where the positive Hund's rule coupling generates high-spin incoherent Hund's metallic states away from half-filling^{55–57}. We consider the semicircular density of state $N(\omega) = \frac{1}{\pi t} \sqrt{1 - [\omega/(2t)]^2}$ with the energy unit set to half-bandwidth $D = 2t = 1$, corresponding to the $\epsilon_{kl\sigma}$ on the Bethe lattice in the limit of infinite coordination¹⁵.

The quasiparticle weight Z for g-RISB and RISB are shown in Fig. 2. From the density plot of the quasiparticle weight in Figs. 2(a) and (b), we found that Hund's metallic regime, characterized by small quasiparticle weight (the purple regime), is much smaller in the original RISB approach. In particular, for electron filling $n = 2$ relevant for Sr_2RuO_4 and iron-based superconductors, the quasiparticle weight is around $Z \gtrsim 0.5$ even with large Coulomb interactions. On the other hand, the quasiparticle weight in g-RISB is about $Z \sim 0.2$ at large Coulomb interactions, which is strongly correlated. In Fig. 2(c) and (d), we show the corresponding quasiparticle weight Z as a function of Coulomb interaction for various filling n . At half-filling $n = 3$, the Mott transition for g-RISB and RISB is at $U_c = 1.25$ and $U_c = 1.6$, respectively. We found that RISB is quantitatively reliable only around half-filling $n = 3$ and becomes less accurate away from half-filling. The overestimation of the quasiparticle weight in RISB, i.e., the underestimation of the effective

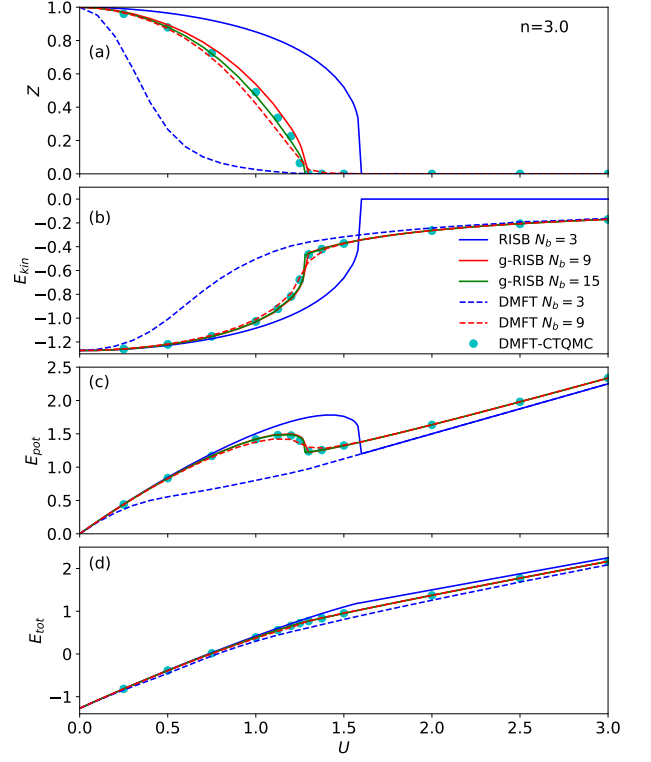


Figure 3. (a) The quasiparticle weight Z , (b) kinetic energy E_{kin} , (c) potential energy E_{pot} , and (d) total energy E_{tot} for the degenerate three-orbital model on Bethe lattice for g-RISB with bath size $N_b = 3, 9, 15$ and DMFT-ED with $N_b = 3, 9$ as a function of Coulomb interaction U with Hund's coupling $J = 0.25U$ at filling $n = 3$. The DMFT-CTQMC results at inverse temperature $\beta = 200$ are shown for comparison. The energy unit is the half-bandwidth.

mass, is also observed in the previous study of Sr_2RuO_4 deviating significantly from the DMFT and experiment value even using larger Coulomb parameters^{24,25}.

We now examine the accuracy of g-RISB closely as a function of Coulomb interactions at half-filling $n = 3$. The corresponding quasiparticle weight Z , kinetic energy E^{kin} , potential energy E^{pot} , and total energy E^{tot} are shown in Fig. 3 for g-RISB, DMFT-ED, and DMFT-CTQMC. We observed that the g-RISB energy and quasiparticle weights converge systematically to the DMFT-CTQMC values with increasing bath orbitals N_b . With bath size $N_b = 9$, g-RISB already gives reliable energy and quasiparticle weights close to the exact DMFT-CTQMC values. On the other hand, the DMFT-ED results still have a slight discrepancy from the exact DMFT-CTQMC values, especially around the metal-insulator transition U_c . Moreover, g-RISB captures more precisely the discontinuity in the quasiparticle weight and the energy at U_c ⁵⁸, and the accuracy in the quasiparticle weight can be further improved by increasing the bath orbitals to $N_b = 15$. To have a closer look at the accuracy of g-RISB, we also show the g-RISB total energy E_{tot} for the selected Coulomb interactions U for different

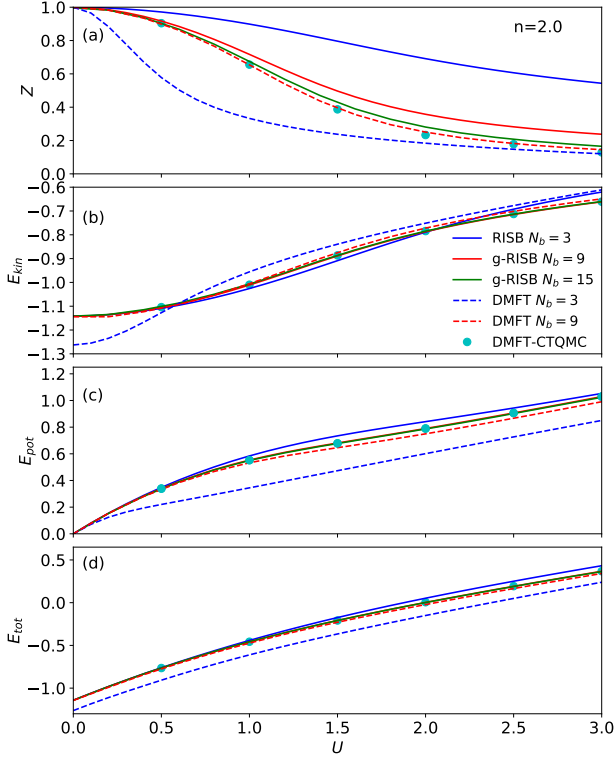


Figure 4. (a) The quasiparticle weight Z , (b) kinetic energy E_{kin} , (c) potential energy E_{pot} , and (d) total energy E_{tot} for the degenerate three-orbital model on Bethe lattice for g-RISB with bath size $N_b = 3, 9, 15$ and DMFT-ED with $N_b = 3, 9$ as a function of Coulomb interaction U with Hund's coupling $J = 0.25U$ at filling $n = 2$. The DMFT-CTQMC results at inverse temperature $\beta = 200$ are shown for comparison. The energy unit is the half-bandwidth.

bath sizes N_b in Tab. I.

In Fig. 4, we also benchmarked the accuracy of g-RISB as a function of Coulomb interactions U at electron filling $n = 2$, corresponding to the parameter regime of Hund's metal materials, e.g., Sr_2RuO_4 and iron-based superconductors. We observed again that the accuracy of g-RISB is systematically improvable with the increasing number of bath orbitals N_b . With $N_b = 9$, g-RISB produces accurate energy close to the exact DMFT-CTQMC values, while DMFT-ED again shows slight differences from the exact DMFT-CTQMC values. On the other hand, DMFT-ED gives accurate quasiparticle weight Z at $N_b = 9$, while g-RISB requires $N_b = 15$ bath orbitals to have similar accuracy. To have a closer look at the g-RISB energy, we show the total energy for the selected parameters in Tab. I.

Figure 5 shows the spectral functions $A(\omega) = -\text{Im}G(\omega)/\pi$ for several sets of parameters at electron filling in the degenerate three-orbital model. For RISB $N_b = 3$, the metal-insulator transition is of the Brinkman-Rice scenario, where only the band renormalization around the Fermi level is captured, and the incoherent Hubbard bands are absent. Therefore, for $n = 3$

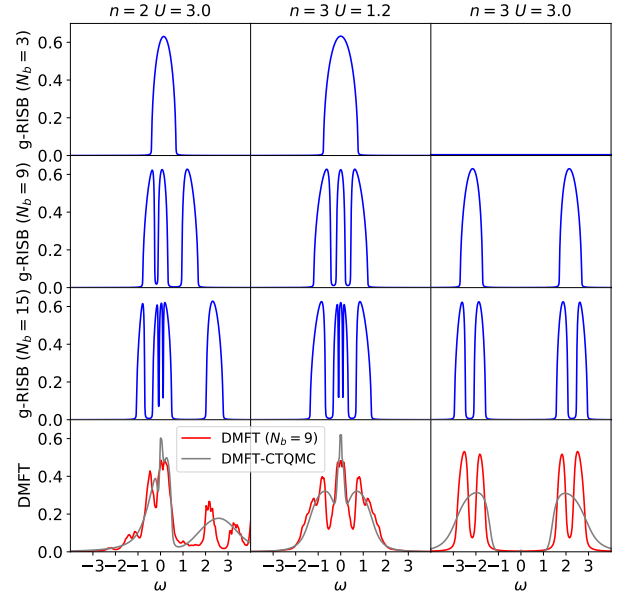


Figure 5. The g-RISB spectral functions $A(\omega)$ with bath size $N_b = 3, 9, 15$ compared with the DMFT spectral function using ED solver with $N_b = 9$ and CTQMC solver for electron filling $n = 2$ and Coulomb $U = 3$ (the first column), $n = 3$ and $U = 1.2$ (the second column), and $n = 3$ and $U = 3$ (the third column). The Hund's coupling is $J = 0.25U$. The inverse temperature in the DMFT-CTQMC calculations is $\beta = 200$, and the energy unit is the half-bandwidth.

| n | U | $N_b = 3$ | $N_b = 9$ | $N_b = 15$ | DMFT-CTQMC |
|-----|-----|-----------|-----------|------------|------------|
| 3.0 | 1.0 | 0.412 | 0.389 | 0.388 | 0.389 |
| 3.0 | 2.5 | 1.875 | 1.774 | 1.773 | 1.772 |
| 2.0 | 1.5 | -0.174 | -0.208 | -0.209 | -0.208 |
| 2.0 | 2.5 | 0.2506 | 0.192 | 0.189 | 0.193 |

Table I. The g-RISB total energy E_{tot} for the degenerate three-orbital model on Bethe lattice for the selected filling n and U with different numbers of bath orbitals N_b and $J = 0.25U$. The DMFT energy at $\beta = 200$ with CTQMC solver is shown for comparison. The energy unit is the half-bandwidth.

and $U = 3$, the spectral function is zero, which is a crude approximation to the Mott insulator. On the other hand, for $N_b = 9$, g-RISB can capture both the coherent quasiparticle peak and the incoherent Hubbard bands, and the quality of the spectral function can be systematically improved by adding more bath orbitals to $N_b = 15$. Furthermore, the overall position of the peaks in the g-RISB spectral functions is in good agreement with the DMFT-ED and DMFT-CTQMC spectral functions. These results suggest that while g-RISB can capture reliable energy, the spectral function requires more bath orbitals to reach a similar accuracy to DMFT-ED.

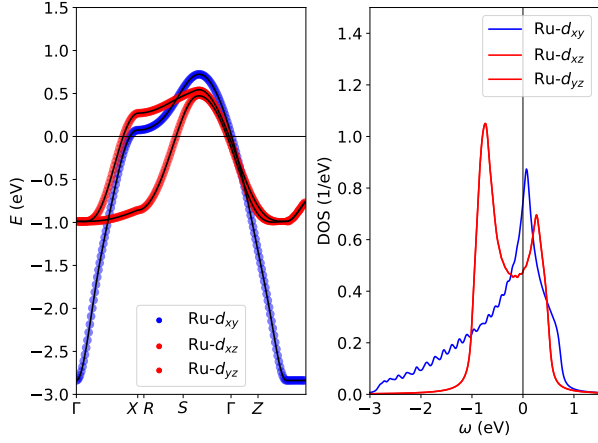


Figure 6. (a) The Wannier tight-binding bandstructure for Sr_2RuO_4 extracted from density functional theory along the high-symmetry path in the Brillouin Zone and (b) the orbital-resolved density of states constructed from the density functional theory considering the $\text{Ru-}d_{xy}$, d_{xz} , and d_{yz} orbitals.

B. Realistic Sr_2RuO_4 model

In this subsection, we present the results for Sr_2RuO_4 , which is a well-characterized bad metal driven by Hund's physics^{59,60}. The experimental quasiparticle weights are $Z_{xz/yz}^{\text{exp}} \sim 0.33$ and $Z_{xy}^{\text{exp}} \sim 0.18$ for the three orbitals in the t_{2g} subshell^{59,61}.

First, we construct the realistic tight-binding model from density functional theory (DFT)^{62,63} and Maximally localized Wannier function⁶⁴. We utilized Wien2k with 10000 k-points and LDA functional for our DFT calculations⁶⁵. The wien2wannier and Wannier90 package is then applied to construct the low-energy tight-binding model^{66,67}. The low-energy model is constructed from the $\text{Ru-}d_{xy}$, d_{xz} , and d_{yz} orbitals with the energy window from -3 eV to 1 eV and $10 \times 10 \times 10$ k-points. The spin-orbit coupling is ignored for simplicity. The Wannier tight-binding dispersion constructed from DFT is shown in Fig. 6. The d_{xz} and d_{yz} show a degenerate quasi-one dimensional density of state, and the d_{xy} orbital has a two-dimensional dispersion with a van Hove singularity at the Fermi level.

Next, we apply RISB to include the electronic correlation effect. Figure 7 (a) and (b) show the momentum-resolved spectral function $A(\mathbf{k}, \omega)$ along the high-symmetry path in the Brillouin Zone and the orbital-resolved density of states for RISB, respectively, at $U = 2.5$ eV and $J = 0.5$ eV. We found that the overall band structure is similar to DFT, with a slight renormalization of the bandwidth. The quasiparticle weights for each orbital are $Z_{xz/yz}^{\text{RISB}} = 0.65$ and $Z_{xy}^{\text{RISB}} = 0.71$, where the values and the ordering are inconsistent with the experiment. This behavior has been reported in Refs. 24 and 25.

We now discuss the g-RISB spectral function and den-

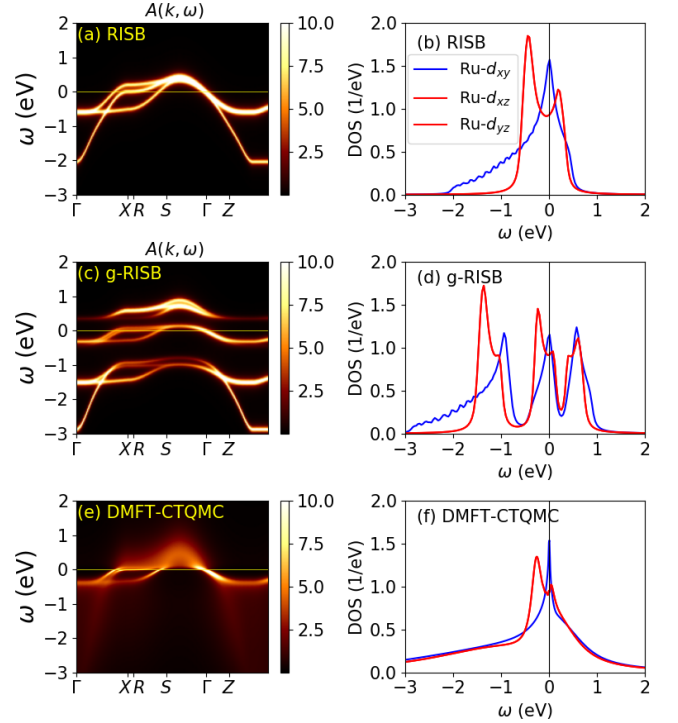


Figure 7. (a) The momentum-resolved spectral function $A(\mathbf{k}, \omega)$ along the high-symmetry path in the Brillouin Zone and (b) the orbital-resolved density of states for Sr_2RuO_4 from RISB with $U = 2.5$ eV and $J = 0.5$ eV. (c) The momentum-resolved spectral function $A(\mathbf{k}, \omega)$ and (d) the orbital-resolved density from g-RISB with bath size $N_b = 9$ at the same Coulomb parameters. (e) The momentum-resolved spectral function $A(\mathbf{k}, \omega)$ and (f) the orbital-resolved density from DMFT with CTQMC solver with $U = 2.3$ eV, $J = 0.4$ eV, and $\beta = 200$ eV^{-1} .

sity of states shown in Fig. 7 (c) and (d), respectively. We use $N_b = 9$ bath orbitals in our g-RISB calculations, so the total number of orbitals in the embedding Hamiltonian is $N_{\text{tot}} = 12$, which can be efficiently solved by ED. The g-RISB band structure contains three groups of bands. The bands around the Fermi-level $\omega = 0$ are the strongly renormalized quasiparticle bands. The quasiparticle weights are $Z_{xz/yz}^{\text{g-RISB}} = 0.33$ and $Z_{xy}^{\text{g-RISB}} = 0.28$ for each orbital in reasonable agreement with the experiment and the DMFT studies^{59,68–72}. The bands located at the energy windows $[-3$ eV, -0.5 eV] and $[0.2$ eV, 0.6 eV] correspond to the lower and upper Hubbard bands, respectively. The DMFT results with CTQMC solver are shown in Fig. 7 (e) and (f), reproducing the previous studies^{71,72}. Our results show that g-RISB is able to accurately capture the low-energy quasiparticle bands around the Fermi level compared to DMFT. On the other hand, although the Hubbard bands in g-RISB locate at the correct energy scales, they do not have the incoherent feature in DMFT, with smeared dispersive bands. We also show the Fermi surface in Fig. 8 for g-RISB with

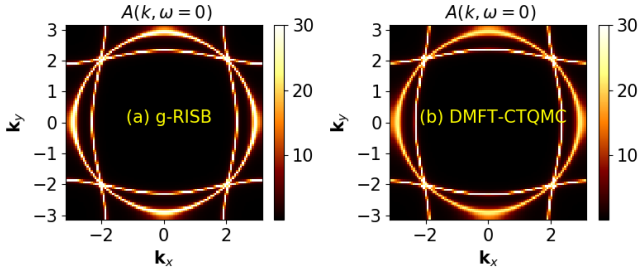


Figure 8. The momentum resolved spectral function for Sr_2RuO_4 at $\omega = 0$, i.e., the Fermi surface, from (a) g-RISB with bath size $N_b = 9$ for $U = 2.5$ eV and $J = 0.5$ eV and (b) DMFT with CTQMC solver for $U = 2.3$ eV and $J = 0.4$ eV and $\beta = 200$ eV $^{-1}$.

| U | $N_b = 3$ | $N_b = 9$ | $N_b = 15$ | DMFT-CTQMC |
|-----|-----------|-----------|------------|------------|
| 1.5 | 3.0895 | 3.056 | 3.055 | 3.053 |
| 2.5 | 6.718 | 6.649 | 6.646 | 6.648 |

Table II. The g-RISB total energy E_{tot} for the Sr_2RuO_4 model with different numbers of bath orbitals N_b at $U = 1.0$ eV and 2.5 eV. The Hund's coupling is $J = 0.2U$, and the electron filling is $n = 4$. The DMFT energy at $\beta = 200$ eV $^{-1}$ with the CTQMC solver is shown for comparison. The energy unit is in electron volts.

$N_b = 9$ and DMFT with CTQMC solver. The g-RISB Fermi surface is in excellent agreement with DMFT.

The quasiparticle weights for g-RISB, RISB, and DMFT as a function of Coulomb interaction U with $J = 0.2U$ are shown in Fig. 9 (a) and (b). The RISB quasiparticle weight is overestimated even at large Coulomb interaction ($Z \sim 0.5$ for $U = 3.0$ eV) compared to the values observed in experiments ($Z_{xz/yz}^{\text{exp}} \sim 0.33$ and $Z_{xy}^{\text{exp}} \sim 0.18$). In addition, the quasiparticle weight in the d_{xy} -orbital is always larger than the $d_{xz/yz}$ -orbitals for all the Coulomb interaction U , which is inconsistent with the experiments and the DMFT values. On the other hand, g-RISB significantly improves the RISB quasiparticle weight towards the DMFT values for the considered interactions U , and the accuracy can be systematically improved with increasing N_b . The kinetic energy E_{kin} and potential energy E_{pot} are shown in Fig. 9 (c) and (d), respectively. We observed that RISB already provides accurate energy for this model, and the energy is almost indistinguishable for g-RISB with $N_b = 9$. To have a closer comparison with DMFT, we also provide the total energy values in Tab. II for the selected parameters.

C. Discussions

The numerical results presented here and in the previous studies on the one-orbital Hubbard model^{26,33–35} strongly suggest that the total energy within g-RISB con-

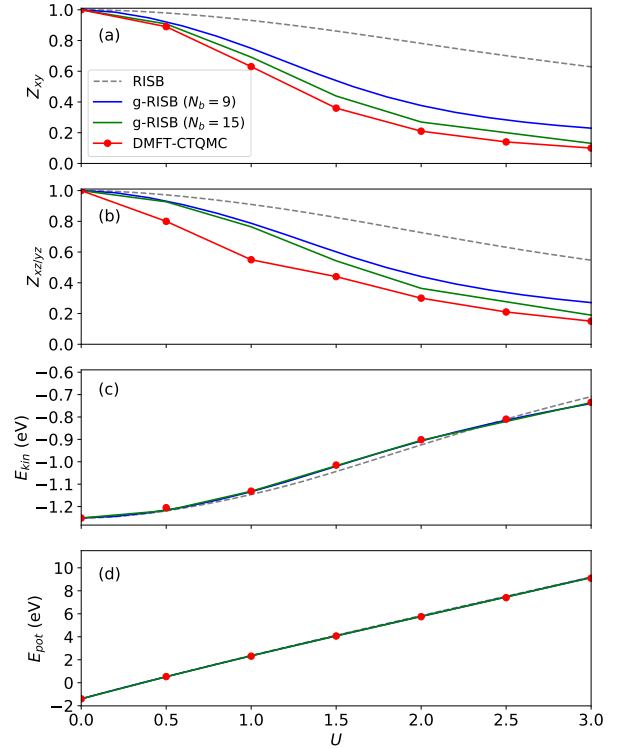


Figure 9. (a) The g-RISB and RISB quasiparticle weight for the xy orbital Z_{xy} , (b) the xz/yz orbital $Z_{xz/yz}$, and (c) the kinetic energy E_{kin} , and (d) the potential energy E_{pot} for Sr_2RuO_4 as a function of Coulomb interaction U with $J = 0.2U$ and bath size $N_b = 3, 9, 15$. The DMFT results with CTQMC solver at $\beta = 200$ eV $^{-1}$ are shown for comparison.

verges to the DMFT total energy from above as the number of ghost orbitals is increased. The g-RISB spectral functions also approach the DMFT spectral functions as the number of bath orbitals in the embedding problem increases. For a given number of bath sites, we observe that g-RISB generally provides more accurate total energy, while DMFT-ED performs better for spectral properties. An analogous situation occurs within electronic structure methods: density functional theory, which targets the exact density of the materials, provides a good approximation to the densities but is less precise for the spectral properties. On the other hand, the more expensive spectral density functional theory, which targets the spectra^{73,74}, yields better results for spectral observables. Likewise, we can view g-RISB as an approximation to an exact density matrix functional theory, which targets the exact one body density matrix⁷⁵, in the same spirit that DMFT can be viewed as an approximation to an exact spectral density functional^{74,76}. From this perspective, we can understand why RISB gives good approximations to the total energies, while the spectra are clearly insufficient as the total spectral weight is too small, and why adding more ghost sites in g-RISB rapidly improves the total energies. The expression of the g-RISB self-energy, which is similar to the DMFT pole expansion (Eq. 17),

calls for further exploration of the connections between these two methods.

V. CONCLUSIONS

We applied the g-RISB approach to the degenerate three-orbital Hubbard and a realistic Sr_2RuO_4 model and benchmarked its accuracy with DMFT. We provide numerical evidence that the accuracy of g-RISB is systematically improvable towards the exact DMFT limit in infinite dimensional multiorbital models with the increasing number of ghost orbitals. This allows a more precise description of Hund's metal behavior and Mott transition compared to the original RISB approach. In addition, we apply g-RISB to a realistic Sr_2RuO_4 model extracted from density functional theory and show that it produces reliable quasiparticle weight, spectral functions, and Fermi surface compared to DMFT and experiments. The connection between the g-RISB and the DMFT self-energy is also discussed.

Our results demonstrate that g-RISB is a promising approach to strongly correlated materials that can be combined with first principle simulations. Moreover, since g-RISB only requires the self-consistent computation of the single-particle density matrix, which circumvents the calculation of Green's function, it is expected to be more efficient than Green's function-based approaches, e.g., DMFT. Future research will focus on the effect of spin-orbit coupling, the development of charge self-consistent DFT+g-RISB^{19,73}, and the accuracy of the g-RISB response functions⁷⁷.

ACKNOWLEDGMENTS

We thank Antoine Georges for useful discussions. T.-H. L, R.A., and G.K. were supported by the U.S. Department of Energy, Office of Science, Office of Advanced Scientific Computing Research, and Office of Basic Energy Sciences, Scientific Discovery through Advanced Computing (SciDAC) program under Award Number DE-SC0022198. This work was supported by the US Department of Energy, Office of Basic Energy Sciences as part of the Computation Material Science Program. N.L. gratefully acknowledges funding from the Simons Foundation (1030691, NL) and the Novo Nordisk Foundation through the Exploratory Interdisciplinary Synergy Programme project NNF19OC0057790.

Appendix A: Convergence of $R^\dagger R$ and $\Sigma(\infty)$

In this appendix, we discuss the convergence of $R^\dagger R$ and $\Sigma(\infty)$ as the number of the bath (ghost) orbitals N_b increases. In Fig. 10, we show the $R^\dagger R$ and $\Sigma(\infty)$ for the degenerate one-orbital $N_{\text{orb}} = 1$, two-orbital $N_{\text{orb}} = 2$, and three-orbital $N_{\text{orb}} = 3$ Hubbard models for the selected Coulomb interaction and electron filling. We use the Hubbard-Kanamori type of Coulomb interaction with Hund's coupling fixed at $J = 0.25U$. Our results demonstrate that $R^\dagger R$ approaches one and $\Sigma(\infty)$ approaches the Hartree-Fock self-energy, indicated by the horizontal lines, with increasing N_b . Note that $R^\dagger R$ and $\Sigma(\infty)$ are degenerate and diagonal matrices in the considered model.

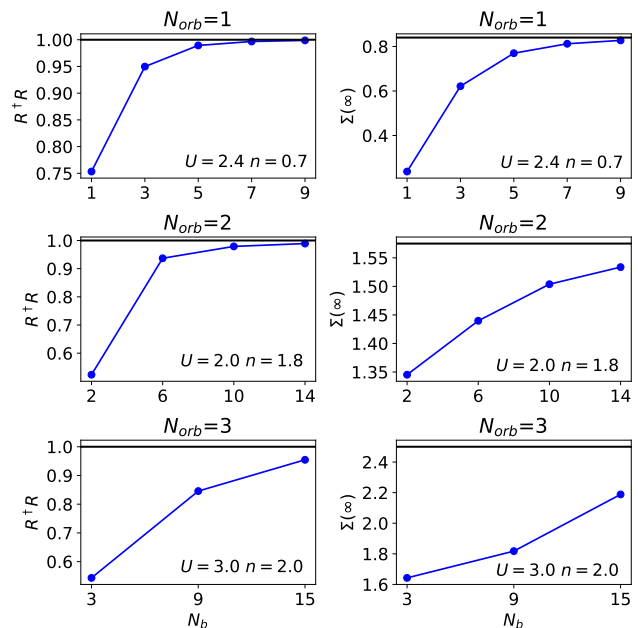


Figure 10. The diagonal element of $R^\dagger R$ and the self-energy at infinity frequency $\Sigma(\infty)$ as a function of the number of the bath orbitals N_b for the degenerate one-orbital $N_{\text{orb}} = 1$, two-orbital $N_{\text{orb}} = 2$, and three-orbital $N_{\text{orb}} = 3$ Hubbard model. The Coulomb parameters U and electron fillings n are given in the figures. The $R^\dagger R$ and $\Sigma(\infty)$ approach one and the Hartree-Fock self-energy (the horizontal lines), respectively.

¹ F. Lechermann, A. Georges, G. Kotliar, and O. Parcollet, Phys. Rev. B **76**, 155102 (2007), URL <https://link.aps.org/doi/10.1103/PhysRevB.76.155102>.

² M. C. Gutzwiller, Phys. Rev. Lett. **10**, 159 (1963), URL <https://link.aps.org/doi/10.1103/PhysRevLett.10.159>.

³ M. C. Gutzwiller, Phys. Rev. **134**, A923 (1964), URL <https://link.aps.org/doi/10.1103/PhysRev.134.A923>.

⁴ W. Metzner and D. Vollhardt, Phys. Rev. Lett. **62**, 324 (1989), URL <https://link.aps.org/doi/10.1103/PhysRevLett.62.324>.

- PhysRevLett. **62**, 324.
- ⁵ J. Bünnemann, W. Weber, and F. Gebhard, Phys. Rev. B **57**, 6896 (1998), URL <https://link.aps.org/doi/10.1103/PhysRevB.57.6896>.
 - ⁶ J. Bünnemann and F. Gebhard, Phys. Rev. B **76**, 193104 (2007), URL <https://link.aps.org/doi/10.1103/PhysRevB.76.193104>.
 - ⁷ M. Fabrizio, Phys. Rev. B **76**, 165110 (2007), URL <https://link.aps.org/doi/10.1103/PhysRevB.76.165110>.
 - ⁸ N. Lanatà, P. Barone, and M. Fabrizio, Phys. Rev. B **78**, 155127 (2008), URL <https://link.aps.org/doi/10.1103/PhysRevB.78.155127>.
 - ⁹ G. Kotliar and A. E. Ruckenstein, Phys. Rev. Lett. **57**, 1362 (1986), URL <https://link.aps.org/doi/10.1103/PhysRevLett.57.1362>.
 - ¹⁰ T. Li, Y. S. Sun, and P. Wölfe, Zeitschrift für Physik B Condensed Matter **82**, 369 (1991), ISSN 1431-584X, URL <https://doi.org/10.1007/BF01357181>.
 - ¹¹ L. de' Medici, A. Georges, and S. Biermann, Phys. Rev. B **72**, 205124 (2005), URL <https://link.aps.org/doi/10.1103/PhysRevB.72.205124>.
 - ¹² M. Crispino, M. Chatzieftheriou, T. Gorni, and L. de' Medici, Phys. Rev. B **107**, 155149 (2023), URL <https://link.aps.org/doi/10.1103/PhysRevB.107.155149>.
 - ¹³ R. Yu and Q. Si, Phys. Rev. B **86**, 085104 (2012), URL <https://link.aps.org/doi/10.1103/PhysRevB.86.085104>.
 - ¹⁴ A. B. Georgescu and S. Ismail-Beigi, Phys. Rev. B **92**, 235117 (2015), URL <https://link.aps.org/doi/10.1103/PhysRevB.92.235117>.
 - ¹⁵ A. Georges, G. Kotliar, W. Krauth, and M. J. Rozenberg, Rev. Mod. Phys. **68**, 13 (1996), URL <https://link.aps.org/doi/10.1103/RevModPhys.68.13>.
 - ¹⁶ X. Deng, L. Wang, X. Dai, and Z. Fang, Phys. Rev. B **79**, 075114 (2009), URL <https://link.aps.org/doi/10.1103/PhysRevB.79.075114>.
 - ¹⁷ N. Lanatà, H. U. R. Strand, X. Dai, and B. Hellsing, Phys. Rev. B **85**, 035133 (2012), URL <https://link.aps.org/doi/10.1103/PhysRevB.85.035133>.
 - ¹⁸ N. Lanatà, Y.-X. Yao, C.-Z. Wang, K.-M. Ho, J. Schmalian, K. Haule, and G. Kotliar, Phys. Rev. Lett. **111**, 196801 (2013), URL <https://link.aps.org/doi/10.1103/PhysRevLett.111.196801>.
 - ¹⁹ N. Lanatà, Y. Yao, C.-Z. Wang, K.-M. Ho, and G. Kotliar, Phys. Rev. X **5**, 011008 (2015), URL <https://link.aps.org/doi/10.1103/PhysRevX.5.011008>.
 - ²⁰ N. Lanatà, Y. Yao, X. Deng, V. Dobrosavljević, and G. Kotliar, Phys. Rev. Lett. **118**, 126401 (2017), URL <https://link.aps.org/doi/10.1103/PhysRevLett.118.126401>.
 - ²¹ N. Lanatà, T.-H. Lee, Y.-X. Yao, V. Stevanović, and V. Dobrosavljević, npj Computational Materials **5**, 30 (2019), ISSN 2057-3960, URL <https://doi.org/10.1038/s41524-019-0169-0>.
 - ²² L. de' Medici, G. Giovannetti, and M. Capone, Phys. Rev. Lett. **112**, 177001 (2014), URL <https://link.aps.org/doi/10.1103/PhysRevLett.112.177001>.
 - ²³ M. S. Frank, T.-H. Lee, G. Bhattacharyya, P. K. H. Tsang, V. L. Quito, V. Dobrosavljević, O. Christiansen, and N. Lanatà, Phys. Rev. B **104**, L081103 (2021), URL <https://link.aps.org/doi/10.1103/PhysRevB.104.L081103>.
 - ²⁴ J. I. Facio, J. Mravlje, L. Pourovskii, P. S. Cornaglia, and V. Vildosola, Phys. Rev. B **98**, 085121 (2018), URL <https://link.aps.org/doi/10.1103/PhysRevB.98.085121>.
 - ²⁵ M. E. Barber, F. Lechermann, S. V. Streltsov, S. L. Skornyakov, S. Ghosh, B. J. Ramshaw, N. Kikugawa, D. A. Sokolov, A. P. Mackenzie, C. W. Hicks, et al., Phys. Rev. B **100**, 245139 (2019), URL <https://link.aps.org/doi/10.1103/PhysRevB.100.245139>.
 - ²⁶ N. Lanatà, T.-H. Lee, Y.-X. Yao, and V. Dobrosavljević, Phys. Rev. B **96**, 195126 (2017), URL <https://link.aps.org/doi/10.1103/PhysRevB.96.195126>.
 - ²⁷ N. Lanatà, Phys. Rev. B **105**, 045111 (2022), URL <https://link.aps.org/doi/10.1103/PhysRevB.105.045111>.
 - ²⁸ E. Fertitta and G. H. Booth, Phys. Rev. B **98**, 235132 (2018), URL <https://link.aps.org/doi/10.1103/PhysRevB.98.235132>.
 - ²⁹ P. V. Sriluckshmy, M. Nusspickel, E. Fertitta, and G. H. Booth, Phys. Rev. B **103**, 085131 (2021), URL <https://link.aps.org/doi/10.1103/PhysRevB.103.085131>.
 - ³⁰ Y.-H. Zhang and S. Sachdev, Phys. Rev. Res. **2**, 023172 (2020), URL <https://link.aps.org/doi/10.1103/PhysRevResearch.2.023172>.
 - ³¹ J. R. Moreno, G. Carleo, A. Georges, and J. Stokes, Proceedings of the National Academy of Sciences **119**, e2122059119 (2022), <https://www.pnas.org/doi/pdf/10.1073/pnas.2122059119>, URL <https://www.pnas.org/doi/abs/10.1073/pnas.2122059119>.
 - ³² D. Guerci, M. Capone, and M. Fabrizio, Phys. Rev. Materials **3**, 054605 (2019), URL <https://link.aps.org/doi/10.1103/PhysRevMaterials.3.054605>.
 - ³³ T.-H. Lee, N. Lanatà, and G. Kotliar, Phys. Rev. B **107**, L121104 (2023), URL <https://link.aps.org/doi/10.1103/PhysRevB.107.L121104>.
 - ³⁴ D. Guerci, Ph.D. thesis, International School for Advanced Studies, <https://iris.sissa.it/handle/20.500.11767/103994> (2019).
 - ³⁵ D. Guerci, M. Capone, and N. Lanata, arXiv:2303.09584 (2023), URL <https://doi.org/10.48550/arXiv.2303.09584>.
 - ³⁶ C. Mejuto-Zaera and M. Fabrizio, arXiv:2305.03329 (2023), URL <https://arxiv.org/abs/2305.03329>.
 - ³⁷ J. Kanamori, Progress of Theoretical Physics **30**, 275 (1963), ISSN 0033-068X, <https://academic.oup.com/ptp/article-pdf/30/3/275/5278869/30-3-275.pdf>, URL <https://doi.org/10.1143/PTP.30.275>.
 - ³⁸ S. R. White, Phys. Rev. Lett. **69**, 2863 (1992), URL <https://link.aps.org/doi/10.1103/PhysRevLett.69.2863>.
 - ³⁹ S. R. White, Phys. Rev. B **48**, 10345 (1993), URL <https://link.aps.org/doi/10.1103/PhysRevB.48.10345>.
 - ⁴⁰ U. Schollwöck, Rev. Mod. Phys. **77**, 259 (2005), URL <https://link.aps.org/doi/10.1103/RevModPhys.77.259>.
 - ⁴¹ Q. Sun, T. C. Berkelbach, N. S. Blunt, G. H. Booth, S. Guo, Z. Li, J. Liu, J. D. McClain, E. R. Sayfutyarova, S. Sharma, et al., WIREs Computational Molecular Science **8**, e1340 (2018), <https://wires.onlinelibrary.wiley.com/doi/pdf/10.1002/wcms.1340>, URL <https://wires.onlinelibrary.wiley.com/doi/abs/10.1002/wcms.1340>.
 - ⁴² Q. Sun, X. Zhang, S. Banerjee, P. Bao, M. Barbry, N. S. Blunt, N. A. Bogdanov, G. H. Booth, J. Chen, Z.-H. Cui, et al., The Journal of Chemical Physics **153**, 024109 (2020), <https://doi.org/10.1063/5.0006074>, URL <https://doi.org/10.1063/5.0006074>.

- ⁴³ H. Zhai and G. K.-L. Chan, The Journal of Chemical Physics **154**, 224116 (2021), <https://doi.org/10.1063/5.0050902>, URL <https://doi.org/10.1063/5.0050902>.
- ⁴⁴ S. Y. Savrasov, K. Haule, and G. Kotliar, Phys. Rev. Lett. **96**, 036404 (2006), URL <https://link.aps.org/doi/10.1103/PhysRevLett.96.036404>.
- ⁴⁵ A. Liebsch, Phys. Rev. Lett. **95**, 116402 (2005), URL <https://link.aps.org/doi/10.1103/PhysRevLett.95.116402>.
- ⁴⁶ C. A. Perroni, H. Ishida, and A. Liebsch, Phys. Rev. B **75**, 045125 (2007), URL <https://link.aps.org/doi/10.1103/PhysRevB.75.045125>.
- ⁴⁷ H. Ishida and A. Liebsch, Phys. Rev. B **81**, 054513 (2010), URL <https://link.aps.org/doi/10.1103/PhysRevB.81.054513>.
- ⁴⁸ A. Liebsch and H. Ishida, Journal of Physics: Condensed Matter **24**, 053201 (2011), URL <https://doi.org/10.1088/0953-8984/24/5/053201>.
- ⁴⁹ M. Capone, M. Civelli, S. S. Kancharla, C. Castellani, and G. Kotliar, Phys. Rev. B **69**, 195105 (2004), URL <https://link.aps.org/doi/10.1103/PhysRevB.69.195105>.
- ⁵⁰ M. Civelli, M. Capone, S. S. Kancharla, O. Parcollet, and G. Kotliar, Phys. Rev. Lett. **95**, 106402 (2005), URL <https://link.aps.org/doi/10.1103/PhysRevLett.95.106402>.
- ⁵¹ B. Kyung, S. S. Kancharla, D. Sénéchal, A.-M. S. Tremblay, M. Civelli, and G. Kotliar, Phys. Rev. B **73**, 165114 (2006), URL <https://link.aps.org/doi/10.1103/PhysRevB.73.165114>.
- ⁵² M. Capone, L. de' Medici, and A. Georges, Phys. Rev. B **76**, 245116 (2007), URL <https://link.aps.org/doi/10.1103/PhysRevB.76.245116>.
- ⁵³ O. Parcollet, M. Ferrero, T. Ayral, H. Hafermann, I. Krivenko, L. Messio, and P. Seth, Computer Physics Communications **196**, 398 (2015), ISSN 0010-4655, URL <http://www.sciencedirect.com/science/article/pii/S0010465515001666>.
- ⁵⁴ P. Seth, I. Krivenko, M. Ferrero, and O. Parcollet, Computer Physics Communications **200**, 274 (2016), ISSN 0010-4655, URL <http://www.sciencedirect.com/science/article/pii/S001046551500404X>.
- ⁵⁵ A. Georges, L. de' Medici, and J. Mravlje, Annual Review of Condensed Matter Physics **4**, 137 (2013), URL <https://doi.org/10.1146/annurev-conmatphys-020911-125045>.
- ⁵⁶ L. de' Medici, J. Mravlje, and A. Georges, Phys. Rev. Lett. **107**, 256401 (2011), URL <https://link.aps.org/doi/10.1103/PhysRevLett.107.256401>.
- ⁵⁷ K. Haule and G. Kotliar, New Journal of Physics **11**, 025021 (2009), URL <http://stacks.iop.org/1367-2630/11/i=2/a=025021>.
- ⁵⁸ M. Chatzieftheriou, A. Kowalski, M. Berović, A. Amaricci, M. Capone, L. De Leo, G. Sangiovanni, and L. de' Medici, Phys. Rev. Lett. **130**, 066401 (2023), URL <https://link.aps.org/doi/10.1103/PhysRevLett.130.066401>.
- ⁵⁹ A. Tamai, M. Zingl, E. Rozbicki, E. Cappelli, S. Riccò, A. de la Torre, S. McKeown Walker, F. Y. Bruno, P. D. C. King, W. Meevasana, et al., Phys. Rev. X **9**, 021048 (2019), URL <https://link.aps.org/doi/10.1103/PhysRevX.9.021048>.
- ⁶⁰ X. Deng, K. Haule, and G. Kotliar, Phys. Rev. Lett. **116**, 256401 (2016), URL <https://link.aps.org/doi/10.1103/PhysRevLett.116.256401>.
- ⁶¹ C. Bergemann, A. P. Mackenzie, S. R. Julian, D. Forsythe, and E. Ohmichi, Advances in Physics **52**, 639 (2003), <https://doi.org/10.1080/00018730310001621737>, URL <https://doi.org/10.1080/00018730310001621737>.
- ⁶² P. Hohenberg and W. Kohn, Phys. Rev. **136**, B864 (1964), URL <https://link.aps.org/doi/10.1103/PhysRev.136.B864>.
- ⁶³ W. Kohn and L. J. Sham, Phys. Rev. **140**, A1133 (1965), URL <https://link.aps.org/doi/10.1103/PhysRev.140.A1133>.
- ⁶⁴ N. Marzari, A. A. Mostofi, J. R. Yates, I. Souza, and D. Vanderbilt, Rev. Mod. Phys. **84**, 1419 (2012), URL <https://link.aps.org/doi/10.1103/RevModPhys.84.1419>.
- ⁶⁵ P. Blaha, K. Schwarz, F. Tran, R. Laskowski, G. K. H. Madsen, and L. D. Marks, The Journal of Chemical Physics **152**, 074101 (2020), <https://doi.org/10.1063/1.5143061>, URL <https://doi.org/10.1063/1.5143061>.
- ⁶⁶ J. KuneÅ, R. Arita, P. Wissgott, A. Toschi, H. Ikeda, and K. Held, Computer Physics Communications **181**, 1888 (2010), ISSN 0010-4655, URL <https://www.sciencedirect.com/science/article/pii/S0010465510002948>.
- ⁶⁷ G. Pizzi, V. Vitale, R. Arita, S. BiÅEgel, F. Freimuth, G. Géranton, M. Gibertini, D. Gresch, C. Johnson, T. Koroetsune, et al., Journal of Physics: Condensed Matter **32**, 165902 (2020), URL <https://doi.org/10.1088/1361-648x/ab51ff>.
- ⁶⁸ J. Mravlje, M. Aichhorn, T. Miyake, K. Haule, G. Kotliar, and A. Georges, Phys. Rev. Lett. **106**, 096401 (2011), URL <https://link.aps.org/doi/10.1103/PhysRevLett.106.096401>.
- ⁶⁹ M. Kim, J. Mravlje, M. Ferrero, O. Parcollet, and A. Georges, Phys. Rev. Lett. **120**, 126401 (2018), URL <https://link.aps.org/doi/10.1103/PhysRevLett.120.126401>.
- ⁷⁰ H. J. Lee, C. H. Kim, and A. Go, Phys. Rev. B **102**, 195115 (2020), URL <https://link.aps.org/doi/10.1103/PhysRevB.102.195115>.
- ⁷¹ F. B. Kugler, M. Zingl, H. U. R. Strand, S.-S. B. Lee, J. von Delft, and A. Georges, Phys. Rev. Lett. **124**, 016401 (2020), URL <https://link.aps.org/doi/10.1103/PhysRevLett.124.016401>.
- ⁷² X. Cao, Y. Lu, P. Hansmann, and M. W. Haverkort, Phys. Rev. B **104**, 115119 (2021), URL <https://link.aps.org/doi/10.1103/PhysRevB.104.115119>.
- ⁷³ G. Kotliar, S. Y. Savrasov, K. Haule, V. S. Oudovenko, O. Parcollet, and C. A. Marianetti, Rev. Mod. Phys. **78**, 865 (2006), URL <https://link.aps.org/doi/10.1103/RevModPhys.78.865>.
- ⁷⁴ S. Y. Savrasov and G. Kotliar, Phys. Rev. B **69**, 245101 (2004), URL <https://link.aps.org/doi/10.1103/PhysRevB.69.245101>.
- ⁷⁵ T. L. Gilbert, Phys. Rev. B **12**, 2111 (1975), URL <https://link.aps.org/doi/10.1103/PhysRevB.12.2111>.
- ⁷⁶ R. Chitra and G. Kotliar, Phys. Rev. B **62**, 12715 (2000), URL <https://link.aps.org/doi/10.1103/PhysRevB.62.12715>.
- ⁷⁷ T.-H. Lee, N. Lanatà, M. Kim, and G. Kotliar, Phys. Rev. X **11**, 041040 (2021), URL <https://link.aps.org/doi/10.1103/PhysRevX.11.041040>.